Developing a shallow-waters finite-differences numerical model to study convectively dominated flows near the boundaries

Guillaume Riflet, Ramiro Neves

Instituto Superior Técnico, Universidade Técnica de Lisboa
Av. Rovisco Pais 1, 1049-001 Lisboa, Portugal
email: guillaume.maretec@ist.utl.pt

Abstract
The shallow water equations are introduced and discretized in a standard C-grid with a leapfrog, face-centred numerical scheme combined with simple Asselin-Roberts filtering. Dirichelet, radiative and closed conditions were implemented at the boundaries. Simple testing were performed with a gaussian level elevation and with wind forcing. The geostrophic equilibrium of a gaussian level elevation is presented and an analytical solution of the steady-state is obtained. Results show that Dirichelet and closed boundary conditions reflect all surface waves back inside the domain and multiple linear superpositions occur, eventually leading to instability. A study on the scalar of Okubo-Weiss is suggested as a diagnostic tool to evaluate hyperbolicity/parabolicity of convectively-dominated flows near open-boundaries.
Keywords: Shallow-Water equations, Okubo-Weiss, Open Boundary Conditions, Geostrophic Equilibrium.

1. Introduction

A 1981 pre-print of a study by Weiss[13] showed that in the regions where the flow was dominantly hyperbolic, the gradients of vorticity would grow exponentially, while in the regions where the flow was dominantly elliptic, the gradients of vorticity would present a periodic behavior. He related this by comparing the squared rate of strain with the squared rate of rotation of the fluid. These quantities can be related to the basic motions of continuous deformation of a continuum medium:

$$\begin{cases} \frac{\partial v}{\partial x} - \frac{\partial u}{\partial y}, & \text{spin} \\ \frac{\partial u}{\partial x} - \frac{\partial v}{\partial y}, & \text{stretch} \\ \frac{\partial v}{\partial x} + \frac{\partial u}{\partial y}, & \text{shear} \\ \frac{\partial u}{\partial x} + \frac{\partial v}{\partial y}, & \text{growth} \end{cases}. \tag{1}$$

These diagnostic quantities, that characterize the advecting field, can be of extreme usefulness to identify the type of motion that a material particle may undergo.

The identity Weiss derives, also presented by Arakawa[1] fifteen years earlier, is equivalent to

$$\frac{\text{shear}^2 + \text{stretch}^2 - \text{spin}^2}{2} = 2\frac{\partial v}{\partial x}\frac{\partial u}{\partial y} - \frac{\partial u}{\partial x}\frac{\partial v}{\partial y} \tag{2}$$

The rate of rotation is identified with vorticity, and its square is identified with enstrophy. Basically, in the regions of the flow where the rate of strain (shear and stress) is dominant, the vorticity is sheared by the hyperbolic flow, while in the regions of the flow where the rate of vorticity is dominant, the vorticity is smoothly advected. Thus the hyperbolic flow is responsible for the growth of the gradients of vorticity. Furthermore, Weiss[13] demonstrated, based on a work by Bourguignon and Brezis[4], that the nature of the flow (elliptic or hyperbolic) is largely influenced by the domain boundary, probably as a consequence that the boundary topology reflects on the Gaussian curvature of the flow's stream function, which Weiss shows to be none other than the rate of strain squared minus the rate of rotation squared (i.e. vorticity squared i.e. enstrophy).

In particular, Weiss demonstrated that for smooth convex boundaries (i.e. the tangent plane to the boundary of the domain D, ∂D, is interior to D at all points on ∂D), the flow is predominantly hyperbolic, while for concave boundaries (i.e. the tangent plane to ∂D is exterior to D i.e. closed domains, bathtubs, pools, etc) the flow is predominantly elliptic in nature, as most classical boundary valued problems are.

These relationships that indicate the influence of the geometry on the flow, and vice-versa, are recurrent and very powerful. In this work, the scalar of Okubo-Weiss (OW) is proposed as a diagnostic

quantity to study convectively dominated problems near open-boundaries. Indeed, boundary-valued numerical problems are solved numerically near open boundaries by choosing one type of boundary condition. It is expected that the OW scalar will help to better quantify the influence of open boundary conditions on the type of flow near the boundaries and provide a solid guideline for numerical modelers to choose the best available boundary condition.

This short work will firstly present a shallow-waters numerical model implemented in Matlab. The model is then validated by considering a simple test-case of the release of a gaussian bump and by comparing numerical results with analytical estimates. Finally, a numerical experiment is devised that exploits the OW scalar to study the influence of passive radiative boundary conditions on the flow near open-bounded regions against an ideal non-bounded flow.

2. Developing a shallow-waters model

The shallow waters equations (SWE) describe the 2D barotropic motion of water masses. The SWE are widely described throughout the literature; for example, they are given in [8] as

$$
\begin{cases}
\frac{\partial Hu}{\partial t} + \frac{\partial Huu}{\partial x} + \frac{\partial Huv}{\partial y} - fHv = & \nu \left(\frac{\partial}{\partial x} \left(H \frac{\partial u}{\partial x} \right) + \frac{\partial}{\partial y} \left(H \frac{\partial u}{\partial y} \right) \right) \\
& -gH \frac{\partial \eta}{\partial x} + \frac{\tau_u^w}{\rho_0} - \frac{\tau_u^b}{\rho_0} \\
\frac{\partial Hv}{\partial t} + \frac{\partial Hvu}{\partial x} + \frac{\partial Hvv}{\partial y} + fHu = & \nu \left(\frac{\partial}{\partial x} \left(H \frac{\partial v}{\partial x} \right) + \frac{\partial}{\partial y} \left(H \frac{\partial v}{\partial y} \right) \right) \\
& -gH \frac{\partial \eta}{\partial y} + \frac{\tau_v^w}{\rho_0} - \frac{\tau_v^b}{\rho_0} \\
\frac{\partial \eta}{\partial t} + \frac{\partial Hu}{\partial x} + \frac{\partial Hv}{\partial y} = 0
\end{cases}
\tag{3}
$$

where H is the depth from the surface level to the bottom, u and v are the zonal and meridional components of velocity, x, y and z are the zonal, meridional and depth positions respectively. $f = 1.01 \times 10^{-4}$ rad/s is the Coriolis frequency at 42° of latitude, ν is the horizontal turbulent viscosity, $g = 9.8$ m^2/s is the gravity acceleration, $\rho_0 = 1033$ kg/m^3 is the water mean density and eta is the water level relative to rest. τ_u^b is the bottom stress zonal component, τ_u^w is the wind stress zonal component. The bottomstress [12] is given by

$$
\tau_u^b = \rho_0 C_D u_b \sqrt{u_b^2 + v_b^2}
$$

where C_D is the bottom drag coefficient and u_b and v_b are the zonal and meridional velocity bottom velocity components. The bottom drag coefficient [11] is given by

$$
C_D = \left(k / \ln \left(\frac{z_D + z_0}{z_0} \right) \right)^2
$$

where z_D is the distance to the bottom , $z_0 = 0.002$ m is a typical roughness length [11] and the Von Karman constant [11] is set to $k = 0.4$. The wind stress [12] is given by

$$
\tau_u^w = \rho_a C_a u_{10} \sqrt{u_{10}^2 + v_{10}^2}
$$

where $\rho_a = 1.25$ kg/m3 is the air density, C_a is an air drag coefficient whose values can be found in [12] and u_{10} and v_{10} is the air speed at 10m height.

2.1. The mesh

The mesh in use is an Arakawa Staggered regular C-grid[1] which consists in staggering three types of regular grids. Each type of grid consists in a regular arrangements of T-cells, U-cells and V-cells. In the T-cell, η and H are evaluated at the centres, and u and v are evaluated at the eastern, western faces and southern, northern faces, respectively. In the U-cell, u is evaluated at the centre, η and H are evaluated at the eastern, western faces, and v is evaluated at the corners. In the V-cell, v is evaluated at the centre, η and H are evaluated at the southern, northern faces, and u is evaluated at the corners. For simplicity, the mesh will have constant step-sizes Δx and Δy. The indices i and j correspond to the i-th zonal cell and the j-th meridional cell counted in the South-North direction and in the West-East direction, respectively.

2.2. The numerical scheme

The spatial finite difference numerical scheme implemented in Matlab for this numerical experiment is

centered in time and centered in time (CTCS), as seen in [8]:

$$\frac{\partial Hu}{\partial t} =$$

$$-\left(m_{U\,i+1} H \left(u_{i+1} + u \right)^2 / 2^2 - m_{U\,i-1} H_{i-1} \left(u + u_{i-1} \right)^2 / 2^2 \right) / \Delta x$$

$$-\left(\begin{array}{l} m_{U\,j+1} \left(H_{i-1} + H_i + H_{i-1,j+1} + H_{i,j+1} \right) \\ \times \left(u_{j+1} + u \right) \left(v_{i-1,j+1} + v_{i,j+1} \right) / 16 \\ -m_{U\,j-1} \left(H_{i-1} + H_i + H_{i-1,j-1} + H_{i,j-1} \right) \\ \times \left(u + u_{j-1} \right) \left(v_{i-1} + v \right) / 16 \end{array} \right) / \Delta y$$

$$+f \left(H + H_{i-1} \right) / 2$$

$$\times \frac{\left(m_V\,v \right)_{i-1} + m_V\,v + \left(m_V\,v \right)_{j+1} + \left(m_V\,v \right)_{i-1,j+1}}{m_{V\,i-1} + m_V + m_{V\,j+1} + m_{V\,i-1,j+1}}$$

$$+\nu \left(m_{U\,i+1} H \frac{u_{i+1} - u}{\Delta x} - m_{U\,i-1} H_{i-1} \frac{u - u_{i-1}}{\Delta x} \right) / \Delta x$$

$$+\nu \left(m_{U\,j+1} H \frac{u_{j+1} - u}{\Delta y} - m_{U\,j-1} H_{j-1} \frac{u - u_{j-1}}{\Delta y} \right) / \Delta y$$

$$-g \left(H + H_{i-1} \right) / 2 \left(\eta - \eta_{i-1} \right) / \Delta x$$

$$+\frac{\rho_a}{\rho_0} C_a u_{10} \sqrt{u_{10}^2 + v_{10}^2}$$

$$-C_D u$$

$$\times \sqrt{u^2 + \left(\frac{\left(m_V\,v \right)_{i-1} + m_V\,v + \left(m_V\,v \right)_{j+1} + \left(m_V\,v \right)_{i-1,j+1}}{m_{V\,i-1} + m_V + m_{V\,j+1} + m_{V\,i-1,j+1}} \right)^2}$$

$$\equiv Ru.$$

m_T, m_U and m_V are land-mask and flux-mask matrices to be described in the next section. For the meridional spatial momentum scheme in the V-Cells, clever symmetry one-to-one relations with zonal momentum scheme in the U-cells are used:

- switch Δx and Δy: $\Delta x \leftrightarrow \Delta y$,

- switch i and j: $i \leftrightarrow j$,

- switch u and v: $u \leftrightarrow v$,

- switch signal of the Coriolis term: $(+ \leftrightarrow -)$.

- switch M and N: $M \leftrightarrow N$,

The finite-difference first-order numerical scheme for the waterlevel (T-Cell) writes out:

$$\begin{aligned} \frac{\partial \eta}{\partial t} &= -\left(m_{T\,i+1} \left(H + H_{i+1} \right) / 2\,u_{i+1} - m_{T\,i-1} \left(H_{i-1} + H \right) / 2\,u \right) / \Delta x \\ &\quad -m_{T\,j+1} \left(\left(H + H_{j+1} \right) / 2\,v_{j+1} - m_{T\,j-1} \left(H_{j-1} + H \right) / 2\,v \right) / \Delta y \\ &\equiv R\eta \end{aligned}$$

The time scheme used is the Leapfrog as described in [8]:

$$\begin{aligned} \eta^{l+1} &= \eta^{l-1} + 2\Delta t \left\{ R\eta \right\}, \\ H^{l+1} &= \eta^{l+1} + d, \\ u^{l+1} &= \left(u^{l-1} \left(H^{l-1} + H_{i-1}^{l-1} \right) + 4\Delta t \left\{ Ru \right\} \right) / \left(H^{l+1} + H_{i-1}^{l+1} \right), \\ v^{l+1} &= \left(v^{l-1} \left(H^{l-1} + H_{j-1}^{l-1} \right) + 4\Delta t \left\{ Rv \right\} \right) / \left(H^{l+1} + H_{j-1}^{l+1} \right). \end{aligned}$$

Notice how the leapfrog time scheme obliges two initial conditions at t_0 and at t_1. Hence, in order to avoid mode decoupling, a Robert-Asselin filter [2] for u, v, η at each integration time-step is used, as suggested by [8]:

$$P^l = P^l + \gamma \left(P^{l-1} - 2P^l + P^{l+1} \right),$$

where γ is a parameter set to 0.1 [8]. The Robert-Asselin provides a good coupling between the two initial conditions, at the expense of some loss in precision [2].

2.3. Boundary conditions
As the SWE differential equations are a boundary-value problem, two main class of boundary conditions were implemented in our numerical solver: null-valued (Dirichelet) and null-flux active boundary conditions, as well as radiative passive boundary conditions. The null-value boundary conditions were implemented by considering that the T-cells have $M \times N$ nodes then the U-cells have $M \times (N+1)$ nodes and the V-cells have $(M+1) \times N$ nodes. η is calculated within $\{2, ..., (M-1)\} \times \{2, ..., (N-1)\}$ and u and v are calculated within $\{2, ..., (M-1)\} \times \{2, ..., N\}$ and $\{2, ..., M\} \times \{2, ..., (N-1)\}$. For the null-fluxes, a land mask, m_T, for the T-cells mesh is introduced. The goal is to impose a null-flux boundary condition surrounding any land cell, i.e.

$$\vec{v} \cdot \vec{n} = 0,$$

where $\vec{v}$ is the velocity vector and $\vec{n}$ is the land/water interface outward normal vector. It returns 1 if the cell is filled with water and 0 if the cell is land. This implies the definition of appropriate null-fluxes masks, m_U and m_V, for the U and V-cells. Thus, for every i, j such that $m_T = 0$, it is required that $m_U = 0$, $m_{U\,i+1} = 0$, $m_V = 0$ and $m_{V\,j+1} = 0$. Everywhere else the value of the masks is 1. The T, U and V masks are to be applied in the numerical scheme to the T-cell properties, the U-cell properties and the V-cell properties, respectively. The radiative scheme is a Flather radiation type [5] implemented follows a NVOE stencil on a C-grid [7]. The *western* boundary radiative condition is defined, for the elevation and the component of velocity perpendicular to the boundary, by

$$\eta_{1,j}^{l+1} = \eta_{1,j} - 2 \frac{\Delta t}{\Delta x} \sqrt{g\, H_{1,j}} \left(\eta_{1,j} - \eta_{2,j} \right),$$

$$u_{1,j}^{l+1} = -\sqrt{\frac{g}{H_{1,j}^{l+1}}} \, \eta_{1,j}^{l+1},$$

for $j = 1, ..., N$, and is defined by, for the velocity component tangent to the boundary,

$$v_{1,j}^{l+1} = \left(\begin{array}{c} v_{1,j} \left(H_{1,j} + H_{1,j-1} \right) \\ -2 \frac{\Delta t}{\Delta x} \sqrt{g \frac{H_{1,j} + H_{1,j-1}}{2}} \left(v_{1,j} - v_{2,j} \right) \end{array} \right) / \left(H_{1,j}^{l+1} + H_{1,j-1}^{l+1} \right),$$

for $j = 2, ..., N$.
For the *eastern* boundary, the radiation boundary condition writes,

$$\eta_{M,j}^{l+1} = \eta_{M,j} - 2 \frac{\Delta t}{\Delta x} \sqrt{g\, H_{M,j}} \left(\eta_{M,j} - \eta_{M-1,j} \right),$$

$$u_{M+1,j}^{l+1} = -\sqrt{\frac{g}{H_{M,j}^{l+1}}} \, \eta_{M,j}^{l+1},$$

for $j = 1, ..., N$, and is defined by, for the velocity component tangent to the boundary,

$$v_{M,j}^{l+1} = \left(\begin{array}{c} v_{M,j} \left(H_{M,j} + H_{M,j-1} \right) \\ -2 \frac{\Delta t}{\Delta x} \sqrt{g \frac{H_{M,j} + H_{M,j-1}}{2}} \left(v_{M,j} - v_{M-1,j} \right) \end{array} \right) / \left(H_{M,j}^{l+1} + H_{M,j-1}^{l+1} \right),$$

for $j = 2, ..., N$. Note that the [5] radiation condition applied to the normal component of velocity to the boundary can be replaced with a simple null-gradient and yield similar results,

$$u_{1,j}^{l+1} = u_{2,j}^{l+1},$$

for $i = 1$, and

$$u_{m+1,\,j}^{l+1} = u_{m,\,j}^{l+1},$$

for $i = m + 1$.

Once more, to derive an adequate scheme for the *southern* and *northern* boundary conditions, simply follow the symmetrical rules below and apply them to the preceding equations

- switch i and j: $i \leftrightarrow j$,

- switch u and v: $u \leftrightarrow v$,

- switch M and N: $M \leftrightarrow N$,

- switch Δx and Δy: $\Delta x \leftrightarrow \Delta y$,

- switch (*West*, *East*) with (*South*, *North*).

3. Validation

The interest of a gaussian level initial condition is that one can test adjustment under gravity of a non-rotating fluid under the hydrostatic approximation, much like the exercise on Gill[6, p. 110]. The hydrostatic approximation simply neglects the vertical velocity and acceleration of the particles to calculate the local pressure. Later on, the Coriolis acceleration can be added, and the flow adjustment under gravity of a rotating fluid can take place, again, much like the exercise on Gill[6, p. 199]. Some basic simulations are set to test the conservation of volume, momentum and vorticity. Even though energy should be conserved when considering the Euler equations, in practice, the numerical viscosity in the model ensures the maintenance of a good rate of dissipation of energy. The interesting thing to test then, is to estimate the rate of energy dissipation. The gaussian initial elevation is given by

$$\eta_{\sigma_x\,\sigma_y}(x,y) = h_0\,e^{-\left(\frac{(x-x_0)^2}{\sigma_x^2} + \frac{(y-y_0)^2}{\sigma_y^2}\right)}, \tag{4}$$

which yields

$$V = \pi\,\sigma_x\,\sigma_y\,h_0, \tag{5}$$

where σ_x, σ_y is the gaussian bell width along the x-axis and the y-axis, x_0, y_0 are the coordinates of the gaussian bell centre, h_0 is the gaussian bell height at it centre and V is its total volume that must be preserved in time (in a closed bathtub-like domain). The integrated available potential energy at the initial instant (APE$_0$), which is equal to the initial total energy (TE$_0$) for an infinite unbounded domain, is calculated to be exactly

$$APE_{0,\,h_0,\,\sigma_x,\,\sigma_y} = \frac{\rho\,g}{4}\,\pi\,\sigma_x\,\sigma_y\,h_0^2. \tag{6}$$

Thus, for a bounded domain sufficiently large relatively to σ_x, Eq (6) gives a good estimative of the TE$_0$, which must be preserved at all times if the domain is closed. The celerity of gravity waves, c, is given, in the shallow water approximation, by [9]

$$c = \sqrt{g\,H}. \tag{7}$$

The characteristic speed of the flow, U, in the gaussian bump initialization, is zero everywhere, except at the wake of the wave front, where the characteristic velocity can be estimated, by geometrical considerations, to be at initial instant

$$U_0 \sim \frac{h_0}{2}\sqrt{\frac{g}{H}}, \tag{8}$$

which would make the Froude number at the wake of the wave to become,

$$\mathrm{Fr} \sim \frac{h_0}{2\,H}. \tag{9}$$

Eq. (8) indicates that the flow velocity in the wake of the wave grows with the initial elevation, which is rather intuitive, but also indicates that the flow velocity reduces as the depth grows, which is rather

counter-intuitive. Hence, the faster the gravity wave celerity, the slower the flow velocity in its wake and the smaller the Froude number. The integrated total energy dissipation rate is given by

$$TE_{,t} = -\int_V \rho \, \epsilon \, dV, \tag{10}$$

where ϵ is the dissipation rate [6]. Considering that the viscous dissipation is a simple turbulence model, then one can infer that the integrated turbulent kinetic energy (TKE) production rate is given by the kinetic energy viscous dissipation rate but with an opposite sign. Furthermore, a plausible estimative of the dissipation rate $\epsilon_\sigma(x, y, t_0)$ for a gaussian bump initial elevation, shortly the initial instant is

$$\epsilon_\sigma(x, y, t_0) = \begin{cases} \nu \left(\frac{U_0}{\sigma}\right)^2, & \text{if } x^2 + y^2 < \sigma \\ 0, & \text{if not.} \end{cases} \tag{11}$$

Integrating Eq. (10) near instant t_0 and using Eq. (11) yields,

$$\frac{TE_{,t}}{TE_0} \equiv -\frac{1}{T_\sigma} = -\frac{\nu}{\sigma^2}, \tag{12}$$

where $T_\sigma = \frac{\sigma^2}{\nu}$ is postulated to be a characteristic time of dissipation of the mechanical energy of the system, which yields the order of magnitude of the time taken for the gaussian bump to dissipate a substancial amount of its initial energy, after being released. It is interesting to notice that it is independent of the gravitic acceleration. Table 1 displays the configuration of the validation experiment, labeled "Validation". Figure 1 displays the time evolution of $\frac{TE}{TE_0}(t^\star)$ for $\nu = 5000$ m^2 s^{-1} in adimensional units of T_σ for several values of σ. The multiple plots show a perfect overlap, indicating that Eq. (12) is plausible. Furthermore, the adimensional time unit of T_σ, given in Eq (12), corresponds roughly to the energy half-life of the system, which is exactly what a characteristic energy dissipation time is expected to yield. The right panel of figure 1 shows a plot of the TE half-life of the system for different viscosities. The plot shows three regions, the low viscosity region for $0 < \nu < 2 \times 10^2$ m^2 s^{-1}, the transition region for $2 \times 10^2 < \nu < 2 \times 10^3$ m^2 s^{-1}, and the high viscosity region for $2 \times 10^3 < \nu < 10^5$ m^2 s^{-1}. For viscosities higher than 10^5 m^2 s^{-1} the system, described in table 1, reaches the limits of its numerical stability. In the low viscosity region there is no dependence of the TE half-life with viscosity, showing a half-life of 3×10^5 s. The low viscosity region is dominated by spurious numerical energy dissipation. Considering the advecting numerical scheme, the numerical energy dissipation is limited as long that the numerical Reynolds number (or numerical Péclet number) as seen in Eq. (13), remains very small.

$$\frac{U \, \Delta x}{2 \, \nu} \ll 1. \tag{13}$$

Furthermore, in the present test-case, the conservation of volume, vorticity and momentum are preserved (not shown) and the perfectly centred initial gaussian water elevation shows a perfect radial symmetry along both X and Y axis (not shown). The conservation of energy is not verified (not shown) due to the artificial numerical viscosity inherent in this type of finite-diferencing technique, seen in Eq. (11). However both the sum of the total energy and the turbulente kinetic energy yield an approximate constant value (not shown).

Table 1: Configurations of the model for a non-rotating and a rotating fluid with a gaussian initial elevation. Three configurations are shown labeled "Validation", "Geostrophy" and "Okubo-Weiss".

Parameter	Validation	Geostrophy	Okubo-Weiss
H	10 m		
h_0	1 cm		
σ_x	6×10^4 m		
ν	0 m^2 s^{-1}	5×10^3 m^2 s^{-1}	
$M \times N$ small model	37×37		
$M \times N$ large model	-	-	73×73
Duration	1.8×10^5 s		8×10^4 s
dx	2×10^4 m		
dt	500 s		
TE_0	2.86×10^9 J		
U_0	$\sim 5 \times 10^{-3}$ m s^{-1}		
c	~ 10 m s^{-1}		
Fr	$\sim 5 \times 10^{-4}$		
Coriolis force	-	yes	-
Boundary	Closed	GWE+FLA	GWE
Volume	1.13×10^8 m^3		
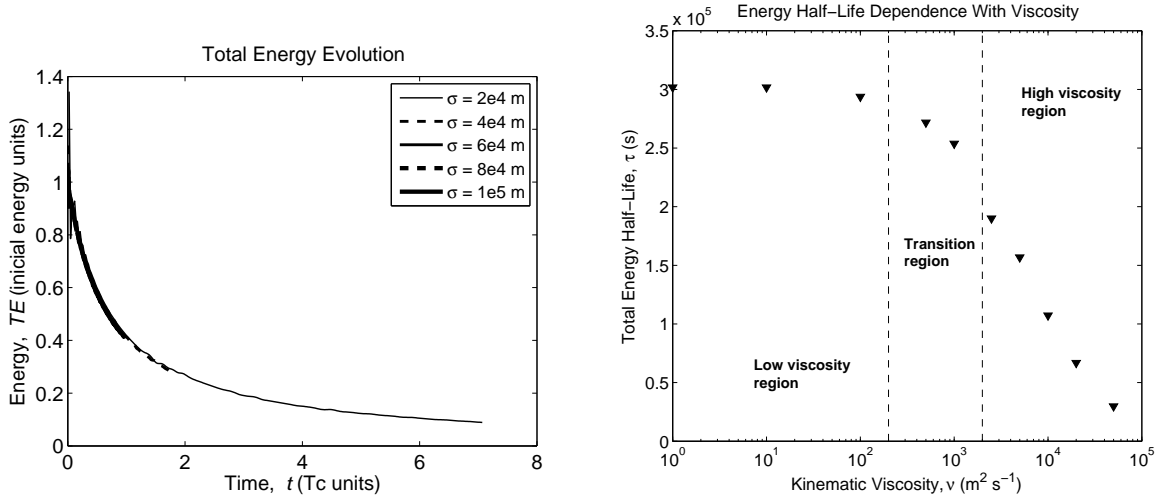
Figure 1: Left panel: evolution of $\frac{TE}{TE_0}$ with $t^\star$ for several values of σ and for a value of $\nu = 5000$ m^2 s^{-1}. The several time-series with the same ν show a perfect overlap. $t^\star = 1$ is equal to T_σ, the characteristic time of dissipation proposed in Eq. (12). Right panel: Dependence of the total energy half-life with viscosity. The viscosity axis is logarithmic. The initial energy of the gaussian bump was 2.86×10^9 J. Three regions are separated by the vertical dashed lines: the low viscosity region for $0 < \nu < 2 \times 10^2$ m^2 s^{-1}, the transition region for $2 \times 10^2 < \nu < 2 \times 10^3$ m^2 s^{-1} and the high viscosity region for $2 \times 10^3 < \nu < 10^5$ m^2 s^{-1}.

4. Geostrophic equilibrium

The following numerical experiments aim at validating and assessing the performance of the simple gravity wave explicit (GWE) radiation condition for the water elevation and for the tangential velocity, and the [5] (FLA) radiation condition for the normal velocity. Table 1 contains the configuration of the "Geostrophy" numerical experiment. The sequence of panels in figure 2 illustrate the geostrophic adjustement of the gaussian bump after release in three stages: a) before the gravity wave front arrives at the boundary, b) during the boundary crossing of the gravity wave and c), after the gravity wave front passed and a geostrophic balance remains. Contrarily to the non-rotating case, after the gravity wave is radiated out of the domain, a significant amount of energy is retained within the geostrophic balance (not shown), about a third of the initial TE, half of which is composed by potential energy coming from the elevation solution at rest and another half which is composed by the geostrophic flow velocity field.
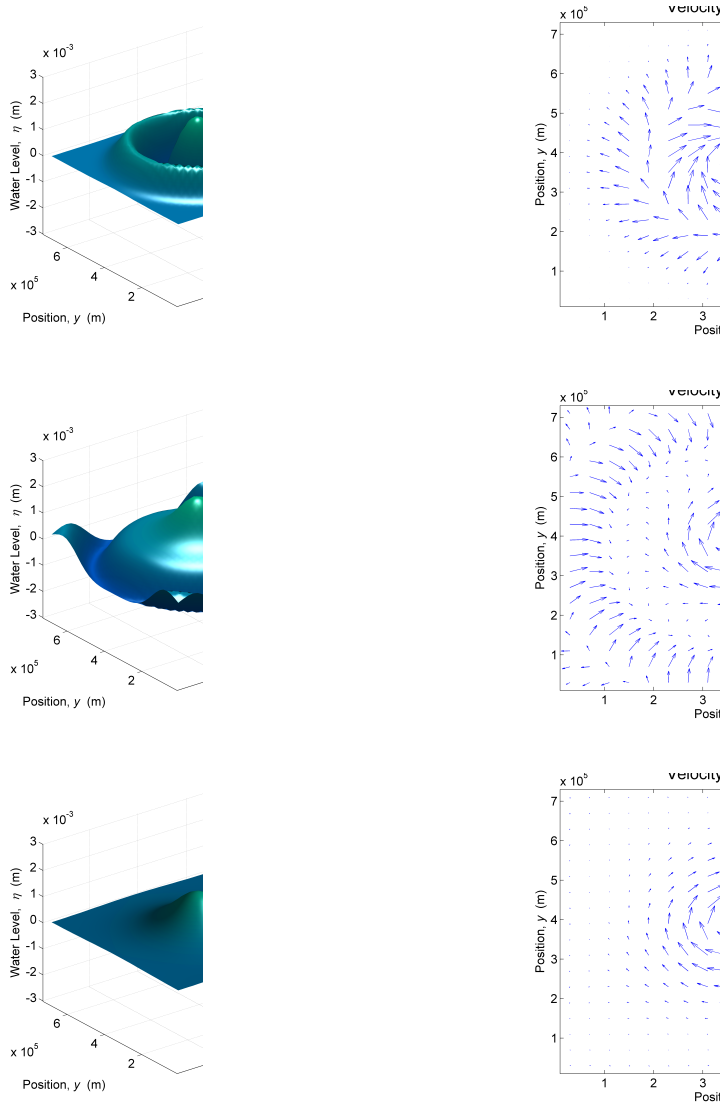
Figure 2: Adjustement of a gaussian elevation in a rotating domain. Left panels display the gravity wave elevation and right panels display the flow velocity field. a) The top panels show the transient state of the system shortly after the initial gaussian elevation was released and before the gravity wave front arrive at the boundaries. b) The middle panels show the gravity wave front crossing the boundaries and the instauration of the central eddy evolving towards geostrophic equilibrium. c) The bottom panels show the geostrophic equilibrium, well after the gravity wave front was radiated at the boundaries.

Geostrophic equilibrium is attained when

$$\begin{cases} f\,v_g = g\,\frac{\partial \eta_g}{\partial x} \\ f\,u_g = -g\,\frac{\partial \eta_g}{\partial y} \end{cases},$$ (14)

where u_g and v_g are the geostrophic components of velocity. Furthermore, it can be demonstrated easily that the geostrophic water elevation, η_g, is the solution of the differential Eq. (15),

$$\frac{\partial^2 \eta_g}{\partial x^2} + \frac{\partial^2 \eta_g}{\partial y^2} = \frac{f^2}{c^2}\,(\eta_g - \eta_0),$$ (15)

where η_0 is the initial water elevation and where the fluid starts from an irrotational state (in the present case, the initial state is the gaussian elevation). Linear differential Eq. (15) is very interesting as it yields a quite simple analytical solution (not shown) that matches well with the numerical solution (not shown).

5. Appying the Okubo-Weiss scalar to assess the open-boundary condition

Besides being an effective tool at identifying eddies, the Okubo-Weiss scalar is fundamentally an objective tool capable of identifying hyperbolic regions of the flow, (dominated by the strain rate tensor, yielding positive values), from elliptic regions of the flow (dominated by vorticity, yielding negative values). The theory goes that solid boundaries (regions of null-flux) influence locally towards an elliptic flow [13]. The idea is to check wether the gravity wave radiative boundary condition influence what otherwise should have been a perfectly hyperbolic flow (i.e. OW < 0). A numerical experiment was setup with two models releasing exactly the same gaussian elevation at their centre. One of the models has the boundaries farther away, thus doubling its grid-cells per dimensional axis. The duration of 80000 s was chosen so that the gravity wave front passed through the smaller domain boundaries but barely reached the larger domain boundaries. The idea is to compare the Okubo-Weiss parameter in the common region of both domains at the same instant of 80000 s. Differences in the nature of the flow should be attributed to the existence of a boundary. Different implementations of boundary conditions should yield differences as well. The goal is to find the best open boundary radiative scheme which yields the most similar OW map with the one from the large domain near the boundaries. The contour plot in figure 3, on the left panel, displays a radial and all positive Okubo-Weiss scalar field with an order of magnitude of about $\sim 10^{-21}$ for the large domain. It means that the flow is purely hyperbolic and has little intensity when compared to the velocity in the wake of the wave front. On the right panel, the OW contour plot in the smaller domain shows an elliptic boundary layer, due to the partial reflection of the gravity wave. The hyperbolic flow on the domain interior reaches $\sim 10^{-19}$, i.e. two orders of magnitude above the flow on the interior of the large domain. This means that the hyperbolic flow of the gravity waves was partially reflected back into the interior of the domain. Objectively, a better radiative boundary condition would minimize or even remove the elliptic boundary layer present in the small domain shown by the Okubo-Weiss parameter.

6. Conclusions

Here lies the shallow-water equations numerical model as described in [8] with the same numerical scheme. It currently only has the Dirichelet boundary conditions and the gravity wave explicit radiation scheme added of a null-gradient or Flather for the normal velocity. This means that, in the former case, all surface waves bounce back at the boundary and and give rise to a cascade of multiple linear superpositions leading to a path of unavoidable numerical instability. In the latter case, the solution radiates any level perturbation (gravitic waves) at the open boundaries [7]. It is important to note that the geometric considerations of the gaussian bump elevation at the instant of release were crucial in order to estimate matching predictions of energy partitioning and production of TKE. In particular, it was found that the relative production rate of TKE varies with viscosity and σ alone, and is independent of the Froude number associated with the gaussian gravity wave. It was also found (Eq. (12)) a characteristic time scale for the energy decay of a two-dimensional wave front. The Okubo-Weiss parameter allowed to quantify the influence of the open boundary condition on the structure of the flow near the boundaries. The numerical evidence shows that boundary conditions tend change local flow from an hyperbolic strucure to an elliptic structure. Further work involves implementing relaxing conditions at the boundaries, variable coriolis force, cyclic boundary conditions. Ultimately, using a sponge layer near the boundaries is considered [10], as well as developing the recent works of [3] with incoming characteristics. A classification of these several boundary conditions using the OW scalar as a quantifier would probably be interesting and useful.
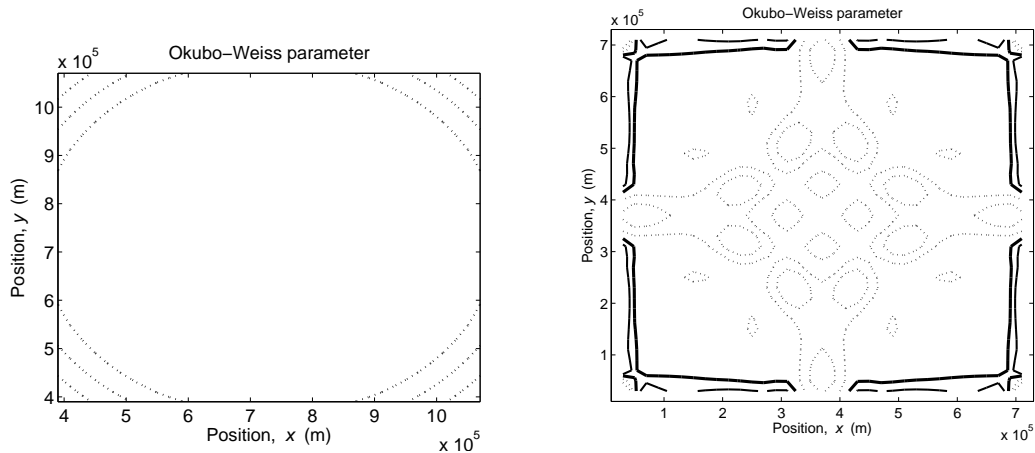
Figure 3: Contour plots of the Okubo-Weiss scalar for the same region. On the left panel, the large domains result. On the right panel, the small domain results. Positive OW contours are dashed and represent hyperbolic flow. Negative OW contours are solid and represent elliptic flow. The null-OW contour is the thick solid line and marks the transition from hyperbolic to elliptic flow.

References

[1] ARAKAWA, A. Computational design for long-term numerical integration of the equations of uid motion: Two-dimensional incompressible ow. Part I. *Journal of Computational Physics 1*, 1 (1966), 119–143.

[2] ASSELIN, R. Frequency filter for time integrations. *Monthly Weather Review 100*, 6 (1972), 487–490.

[3] BLAYO, E., AND DEBREU, L. Revisiting open boundary conditions from the point of view of characteristic variables. *Ocean Modelling 9* (2005), 231–252.

[4] BOURGUIGNON, J. P., AND BREZIS, H. Remarks on the euler equation. *Journal of functional analysis 15*, 4 (1974), 341–363.

[5] FLATHER, R. A. A tidal model of the northwest European continental shelf. *Mem. Soc. R. Sci. Liege 10*, 6 (1976), 141–164.

[6] GILL, A. E. *Atmosphere-ocean dynamics*. Academic Press New York, 1982.

[7] HERZFELD, M. The role of numerical implementation on open boundary behaviour in limited area ocean models. *Ocean Modelling 27*, 1-2 (2009), 18–32.

[8] KANTHA, L. H., AND CLAYSON, C. A. *Numerical models of oceans and oceanic processes*. Academic Press, 2000.

[9] KUNDU, P. K., AND COHEN, I. M. *Fluid mechanics*. Academic Press San Diego, 2002.

[10] LAVELLE, J. W., AND THACKER, W. C. A pretty good sponge: Dealing with open boundaries in limited-area ocean models. *Ocean Modelling 20*, 3 (2008), 270–292.

[11] LEITÃO, P. C. *Integration of Scales and Processes in the marine Environment Modelling*. PhD thesis, Technical Superior Institute, Lisbon, 2003.

[12] PIETRZAK, J., JAKOBSON, J. B., BURCHARD, H., VESTED, H. J., AND PETERSEN, O. A three-dimensional hydrostatic model for coastal and ocean modelling using a generalised topography following co-ordinate system. *Ocean Modelling 4*, 2 (2002), 173–205.

[13] WEISS, J. The dynamics of enstrophy transfer in two-dimensional hydrodynamics. *Physica D Nonlinear Phenomena 48* (March 1991), 273–294.